Int. J. Electrochem. Sci., 13 **(2018)** 8803 – 8816, doi: 10.20964/2018.09.25

International Journal of ELECTROCHEMICAL SCIENCE
www.electrochemsci.org

Stability and Sulfur resistance of Y-doped $La_{0.7}Sr_{0.3}CrO_3$: a promising Solid-Oxide-Fuel-Cell anode

Xiufang Zhu[1,*], *Linzhi Zhai*[2], *Lijing Zhang*[1], *Lei He*[1], *Jie Song*[3]

[1] National & Local Joint Engineering Research Center for Deep Utilization Technology of Rock-salt Resource, Huaiyin Institute of Technology, Huaian, 223003, China.
[2] School of Environment and Chemical Engineering, Jiangsu University of Science and Technology, Zhenjiang, 212205, China.
[3] Jiangsu Key Laboratory for Biomass-based Energy and Enzyme Technology, School of Chemistry and Chemical Engineering, Huaiyin Normal University, Huaian 223300, China
[*]E-mail: xiufangzhu@163.com

Received: 15 April 2018 / *Accepted:* 13 june 2018 / *Published:* 5 August 2018

Perovskite-type of Y-doped $La_{0.7}Sr_{0.3}CrO_3$ as a promising anode for solid oxide fuel cell, maintain good stability in H_2S-containing atmosphere based on the results from the X-ray diffraction patterns and Fourier transform infrared spectroscope in our previous work. In the research explore the single cell performance and reveal its sulfur durability under the real H_2S environment. The activity of the anode has a close relationship with its material composition, the crystal structure and the morphologic structure, etc. Therefore, Y-doped $La_{0.7}Sr_{0.3}CrO_3$ as the anode material is further investigated by XRD, high-resolution transmission electron microscopy and scanning electron microscopy. The surface composition and valence of each element in Y-doped $La_{0.7}Sr_{0.3}CrO_3$ are identified by X-ray photoelectron spectroscopy. Thermodynamic calculation is used to analyze the stability of each element in Y-doped $La_{0.7}Sr_{0.3}CrO_3$ when it is exposed in H_2S at the range of partial pressures of sulfur (pS_2) and (pO_2) simulated the fuel cell conditions. Meanwhile, the single cell with configuration Y-doped $La_{0.7}Sr_{0.3}CrO_3$-SDC/SDC/Ag is measured under real H_2S atmosphere at 600, 650 and 700 ℃ for verification of the simulation. Then the electrochemical impedance spectrum is used to analyze the reasons that affected cell performance.

Keywords: Solid oxide fuel cell, Y-doped $La_{0.7}Sr_{0.3}CrO_3$ anode, Sulfur tolerance, Hydrogen sulfide

1. INTRODUCTION

Solid oxide fuel cells (SOFCs) are regarded as a promising clean energy conversion system because of high-energy conversion efficiency, efficient reclamation of waste heat, low environment impact, and extensive fuel flexibility compared to other fuel cells [1-4]. However, even with these benefits, the high operating temperature (800-1000 ℃) causes several problems, e.g., expensive maintenance cost, material degradation, and material compatibility challenges [5, 6]. Reducing the operating temperature to below 700 ℃ has received considerable attention. However, a series of problems ensued, including the performance dropped drastically as the rapid increasing in polarization losses (associated with low electrolyte conductivity and poor electrodes reactions kinetics) [7].

The feasibility of using H_2S as the fuel for a SOFC simultaneously produces electricity[8,9]. However, the toxicity of H_2S to anode materials for SOFC is catastrophic. Searching for sulfur-resistant anode materials is a challenge to develop SOFC.

Perovskite-type oxide with a general formula of ABO_3 (Typical material is $LaCrO_3$) has played an important role for application in SOFCs for A-site and B-site replaced by other ions that can improve the physical properties [10-12]. $LaCrO_3$ as electrode materials have been extensively investigated [13, 14]. Due to the material of A Ca- and Co-doped yttrium the excellent property as anode materials such as improving chemical and dimensional stability in hydrogen with 3% H_2O and 10-20 ppm H_2S [15-17]. Our previous investigation confirmed that Y doped $La_{0.7}Sr_{0.3}CrO_3$ can be used as a potential anode for its high electrical performance [12]. Tan etc [18] indicated that the doped of non-variant valence metal Y can increase the tolerant to sulfur, but the reason of the stability and sulfur resistance was not explained clearly. So in the paper, the stability and the sulfur durability of Y doped $La_{0.7}Sr_{0.3}CrO_3$ under the real H_2S environment was investigated from microstructure, the surface composition and valence of each element before and after single cell test.

2. EXPERIMENT

A serial of $La_{0.7-x}Y_xSr_{0.3}CrO_3$ (x=0.1, 0.13, 0.15, 0.17, 0.2) were synthesized by urea combustion method. The details of the synthesis have been described in our previously study [11]. The precursor ashes were calcined in the air at 1350 ℃ for 4 h using a rate of 5 ℃ min^{-1}.

The crystalline structure of the anode materials was examined by X-ray diffraction patterns (XRD, Bruker D8 Advance, Germany) using Cu K_α radiation (λ=0.15406) at room temperature with 2θ ranging from 5° to 80°. Temperature-programmed reduction using hydrogen (H_2-TPR) was performed at atmospheric pressure in a continuous flow reactor charged with 25 mg of sample powders. H_2-TPR tests were performed with 10% H_2 in Ar at a flow rate of 30 $ml\cdot min^{-1}$, heated from room temperature to 900 ℃ at a rate of 10 ℃ min^{-1} and then held at 900 ℃ for 30 min.

Temperature-programmed reduction (TPR) was carried out with the Quanta Chembet (3000) instrument. 0.1g fresh samples were performed with a 10% H_2-N_2 flow (70mL/min) heating from room temperature to 900 ℃ for 1 h. The H_2 consumption was determined by a TCD detector, while ice was trapped in a cold trap.

Due to the good single crystal structure and stability in the reducing atmosphere, $La_{0.7-x}Y_xSr_{0.3}CrO_3$ (x=0.13) was selected to investigate the sulfur tolerance of LYSC from the microstructure and morphologies by scanning electron microscopy (SEM, S-4800Ⅱ FESEM, Japan), high-resolution transmission electron microscopy (HRTEM, JEM-2100F), selected-area electron diffraction (SAED). The surface composition and valence of each element were identified by X-ray photoelectron spectroscopy (XPS, Themo ESCALAB 250, US).

Electrochemical workstation was used to measure the performance of the single cell with configuration LYSC-SDC/SDC/Ag under real H_2S atmosphere at 600 to 700 ℃ for verification of the simulation. Then the electrochemical impedance spectrum (EIS) was used to analyze the reasons that affected cell performance.

3. RESULTS AND DISCUSSION

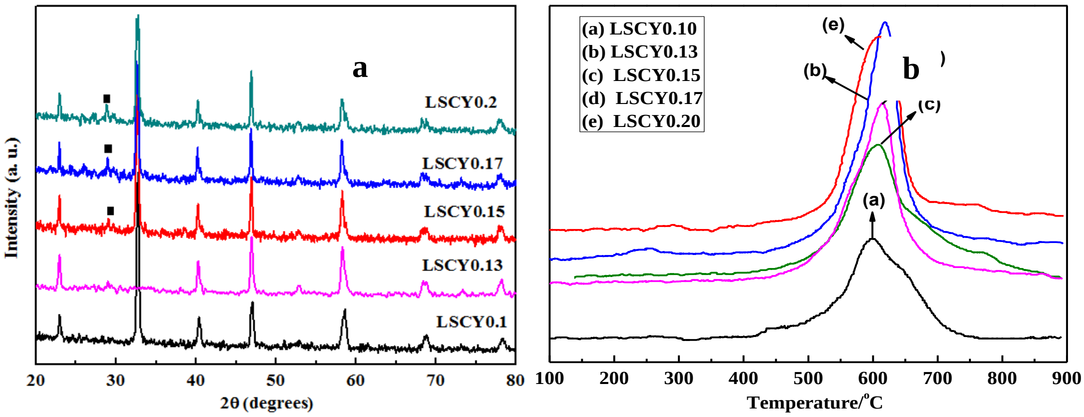

Figure 1. (a) XRD patterns and (b) H_2-TPR curves of $La_{0.7-x}Y_xSr_{0.3}CrO_3$ (x=0.1, 0.13, 0.15, 0.17, 0.2)

Figure 1(a) showed the XRD patterns with different content of Y (x=0.1, 0.13, 0.15, 0.17 and 0.2) after firing in air at 1350 ℃ for 4 h, suggesting that when the value of x>0.13, some impure peaks ($SrCrO_4$) appeared. Resistance against thermal and chemical reduction for the samples was further studied by H_2-TPR with the results shown in Figure 1(b). The TPR profile of Y doped $La_{0.7}Sr_{0.3}CrO_3$ had reduction α peaks at about 600 ℃ when x=0.1, 0.2. The other values of x also had the α peaks at about 610 ℃, the reduction temperature was changed according to the doped of Y. According to the Reference [19], the reduction peaks which appeared between 550 and 700 ℃ were attributed to the reduction of Cr^{4+} to Cr^{3+}. The small shoulder peaks appeared about 470 ℃ were assigned to the reduction of Cr^{6+} to Cr^{4+}. Among the peaks, when the value of x=0.13, the corresponding peak moved to a higher temperature zone, suggesting greater chemical stability of the LYSC. From the analysis of XRD and H_2-TPR, x=0.13 (that is $La_{0.57}Y_{0.13}Sr_{0.3}CrO_{3\pm\delta}$, abbrev. LYSC13) as the best candidate was chosen in the following study.

As shown in Figure 2, the pure perovskite phase can be formed at 1350 ℃ from the XRD patterns of all the calcined LYSC13. The diffraction pattern for the electrode posited film has eleven broad peaks at $2\theta=23.022^{\circ}$, 32.785°, 40.442°, 47.045°, 53.003°, 58.524°, 68.725°, 73.548°, 78.255°, 82.882° and 87.462°, corresponding to (100), (110), (111), (200), (210), (211), (220), (221), (310), (311) and (222) of $La_{0.8}Sr_{0.2}CrO_3$ (JCPDS card no. 74-1980), respectively. While some impurity peaks are observed in the sample at 2θ=29.169 and 48.528 degrees (marked with *), which are characteristic of the Y_2O_3 parent (JCPDS card No. 76-0151) after calcined at 1150 ℃. Therefore, 1350 ℃ was chosen as the calcination temperature.

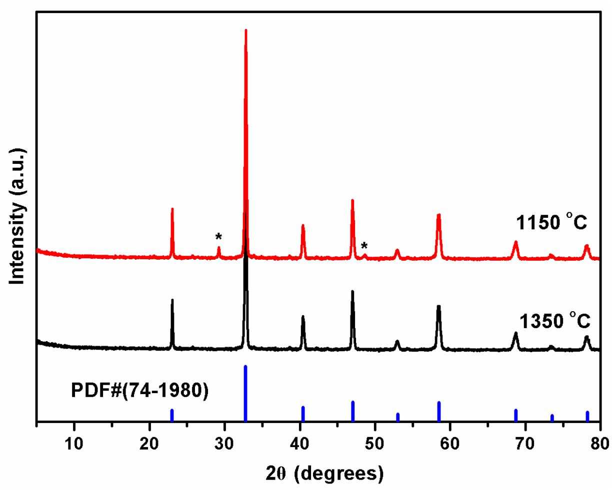

Figure 2. X-ray diffraction patterns of LYSC13 at 1150 and 1350 ℃

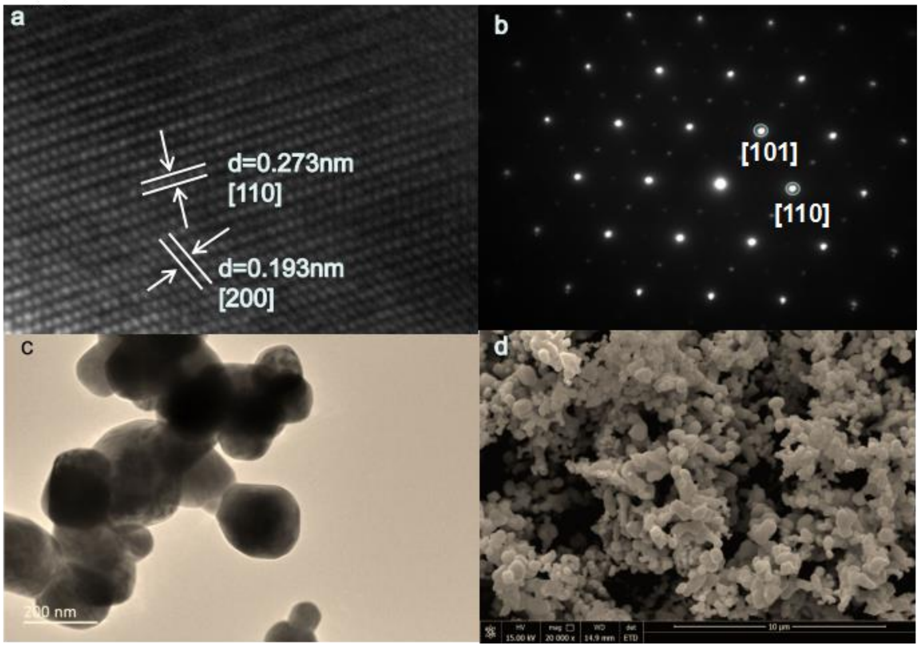

Figure 3. Experimental SAED patterns of LYSC13 crystal along the (a) [110], (b)[111]. Experimental HRTEM images of the crystal as shown in (c) and SEM images of the LYSC13 as shown in (d).

TEM and SEM images in Figure 3c and 3d showed the morphology of LYSC13. LYSC13 could be indexed according to the cubic perovskite structure with a lattice parameter of a ~2.5 Å. The SEM images of LYSC13 also showed essentially the porous surface morphology composing of particles, indicating that each particle was a LYSC13 single crystal since the structure similar to the one calculated from the HRTEM results. The most symmetric space groups *Pm3m* was selected by fitting of the XRD profile. HRTEM was conducted to further investigate the structural and elemental characters. The clear Moire fringes and split points in the corresponding fast Fourier transform (FFT) pattern in samples demonstrated the single-crystalline nature of the surface as shown in Figure 3a and 3b. The lattice fringes of LYSC13 displayed interplanar spacings of 0.273 and 0.193 nm in the particle, which matched well respectively with those of the [110] and the [200] planes of the fcc LYSC13 anode materials and the results were agreement with XRD patterns. A selected area electron diffraction (SAED) pattern along the [111] zone axes and no different grains were observed as shown in Figure 3a, 3b. The relatively high intensity streaks along [111] in the [110] diffraction pattern (as shown in Figure 3b) were observed for some grains, which would be regarded as B-site cation (Cr(Ⅲ) and Cr(Ⅳ)) ordering for the overlap of stacking fault-derived scattering [20, 21], or as the ordering of oxygen vacancies [22], which were in agreement with the XPS results.

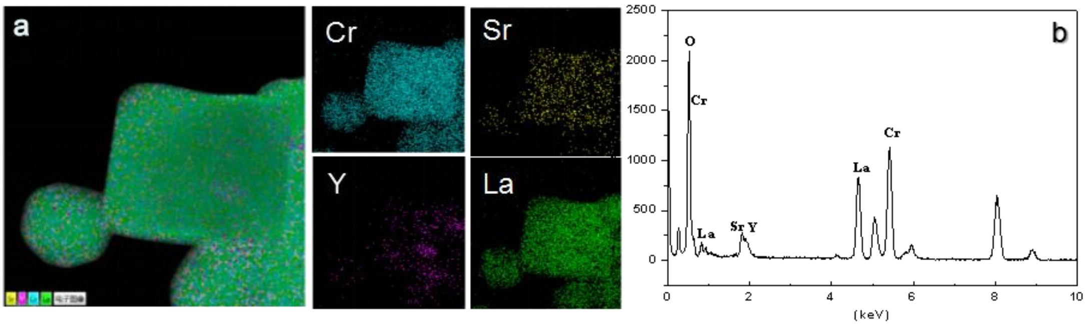

Figure 4. EDS mapping of LYSC13

The elemental mapping images in Figure 4a clearly pointed out a highly uniform distribution of Cr, Sr, Y and La, confirming the formation of an embedded of Sr and Y in the porous $LaCrO_3$. Figure 4b showed the energy dispersive spectrum (EDS). The results reveal the existence of La, Y, Sr, Cr, O and Cu (8 keV) elements, wherein the Cu signal was ascribed to the copper grid used in the process of testing.

Fuel cell tests were measured to estimate the electrochemical activity of the anode material. I-V and I-P curves of single cell with configuration of LYSC13-SDC/SDC/Ag under the operation temperatures (10% H_2-0.1% H_2S, other was N_2 as balance gas) were given in Figure 5a. The power densities were 18.52, 56.05 and 62.66 $mWcm^{-2}$ at 600, 650 and 700 ℃, respectively. The corresponding OCV values were 0.90, 0.94 and 0.96 V. The impedance spectroscopy was employed to analyze the effect of operating temperature on single cells as shown in Figure 5b. The impedance spectra are mainly composed of two sections. One is the ohmic resistance (R_{ohm}) (which is located at high frequency) which mainly include electrolyte resistance, the electrode ohmic resistance, the connector resistance, the lead resistance and other contact resistances, etc. Another is the activation resistance (R_{act}) which is located at low frequency, including cathode, anode activation polarization resistance and concentration polarization resistance. Figure 5b showed that the R_{ohm} varies slightly with the temperatures, while a large change occurred in the R_{act}. Therefore, the main loss of the fuel cell was due to the electrode polarization.

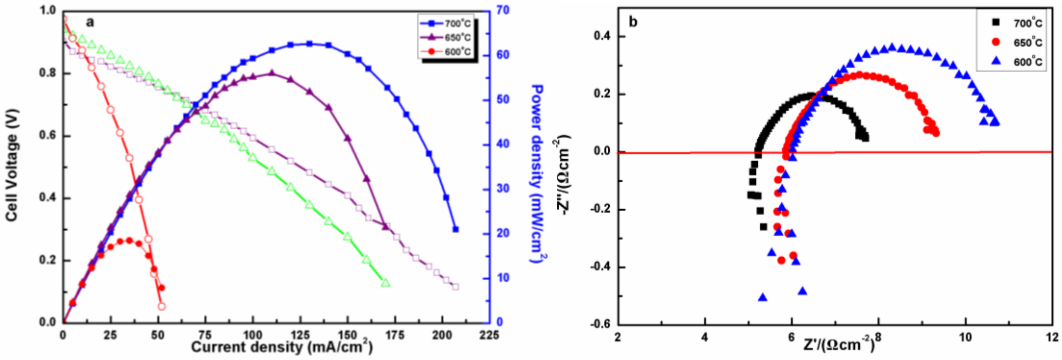

Figure 5. IV-IP and the impedance spectroscopy of LYSC13 as anode under 10% H_2-1% H_2S fuel at different temperatures

Within the work atmosphere and temperature, the anode material needs to have enough high electrical conductivity to ensure that the anode material has good conductivity performance, so as to making the electronic from electrochemical reaction passed to the external circuit and further generating the current. In addition, the anode catalyst must have a high ionic conductivity, so that the fuel can arrive to the anode area for electrochemical reaction. The conductivity of LYSC13 were measured by 4-probe DC in 10% H_2-0.1% H_2S from 500 to 800 ℃. In LYSC13, the substitution of Sr for La or Y resulted in a charge-compensation transition of Cr^{3+} to Cr^{4+}, which gives rise to the formation of small polaron as charge carries and thermally activated hopping as the transport mechanism [23]. The conductivities increased with the temperature rising as shown in Figure 6. The behavior was typical small polaron mechanism and can be expresses as

$$\sigma = (A/T)\exp(-E_a/kT)$$

where *A* is the pre-exponential factor, E_a is the activation energy, *k* is the Boltzmann constant, and *T* is the absolute temperature.

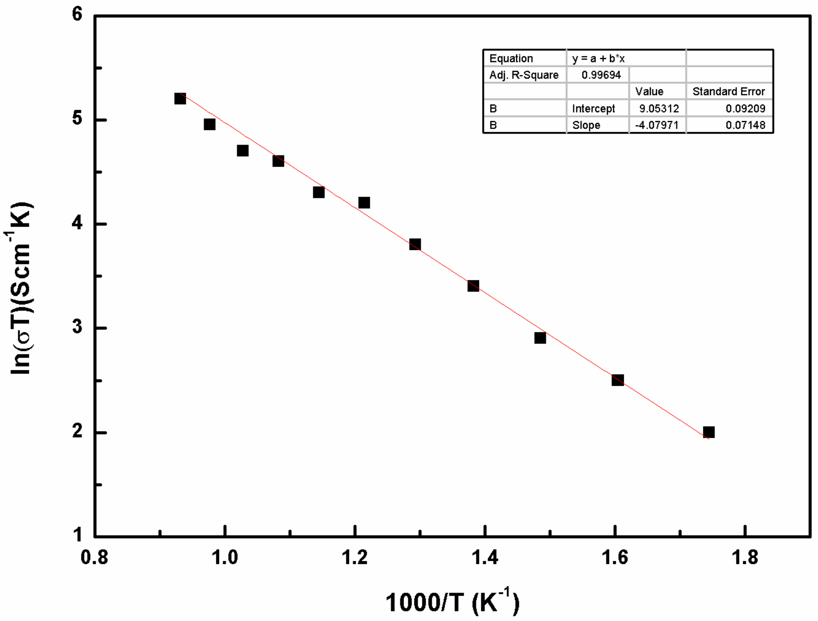

Equation	y = a + b*x		
Adj. R-Square	0.99694		
		Value	Standard Error
B	Intercept	9.05312	0.09209
B	Slope	-4.07971	0.07148

Figure 6. Ln(σT) for LYSC13 as a founction of 1000/T

The long-term galvanostatic test of the single cell at 700 ℃ was given in Figure 7. The OCV started to stabilize after the single running 2 h, ascribed to conditioning of the anode catalyst, and there were no detectable sulfides on the anode surface as determined by the XPS analysis after cooling to room temperature.

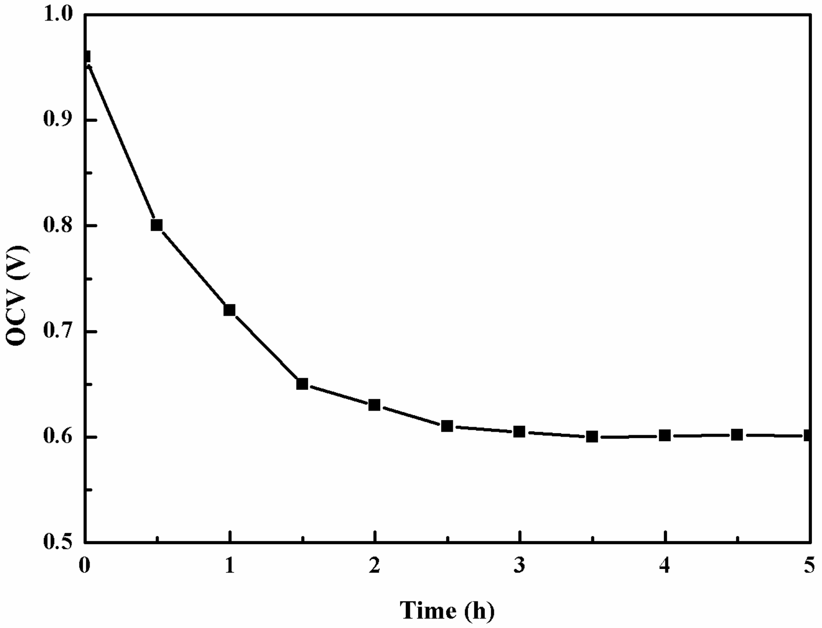

Figure 7. Long-term galvanostatic test the single cell LYSC13/SDC/Ag at 700 ℃

Table 1. The partial pressure of O_2 (g) and S_2 (g) under the operation condition

t/℃	Partial pressures input boundary /Pa			Partial pressures output boundary /Pa		
	O_2	S_2 at $w(H_2S)$ of 1×10^{-6}	S_2 at $w(H_2S)$ of 1×10^{-2}	O_2	S_2 at $w(H_2S)$ of 1×10^{-6}	S_2 at $w(H_2S)$ of 1×10^{-2}
600	4.83×10^{-28}	1.08×10^{-19}	1.08×10^{-11}	4.09×10^{-23}	1.02×10^{-17}	1.02×10^{-9}
650	1.78×10^{-26}	1.47×10^{-19}	1.47×10^{-11}	1.51×10^{-21}	1.38×10^{-17}	1.38×10^{-9}
700	4.55×10^{-25}	1.49×10^{-17}	1.49×10^{-9}	3.85×10^{-20}	1.4×10^{-15}	1.4×10^{-7}

In order to consider elements interacting in the anode material, the thermodynamic calculations were used to analyse the phase diagrams of La-O-S, Y-O-S, Sr-O-S and Cr-O-S. According to the Reference [24], the values of pO_2(g) and pS_2(g) were defined by assuming a mixture 3% H_2O and 97%

H_2 as the input fuel to the anode, and 90% H_2O and 10% H_2 mixture as the output gases which represented the fuel consumption of H_2 with 90% in SOFC. The partial pressure of O_2 (g) and S_2 (g) under the operation condition was calculated as shown in Table 1.

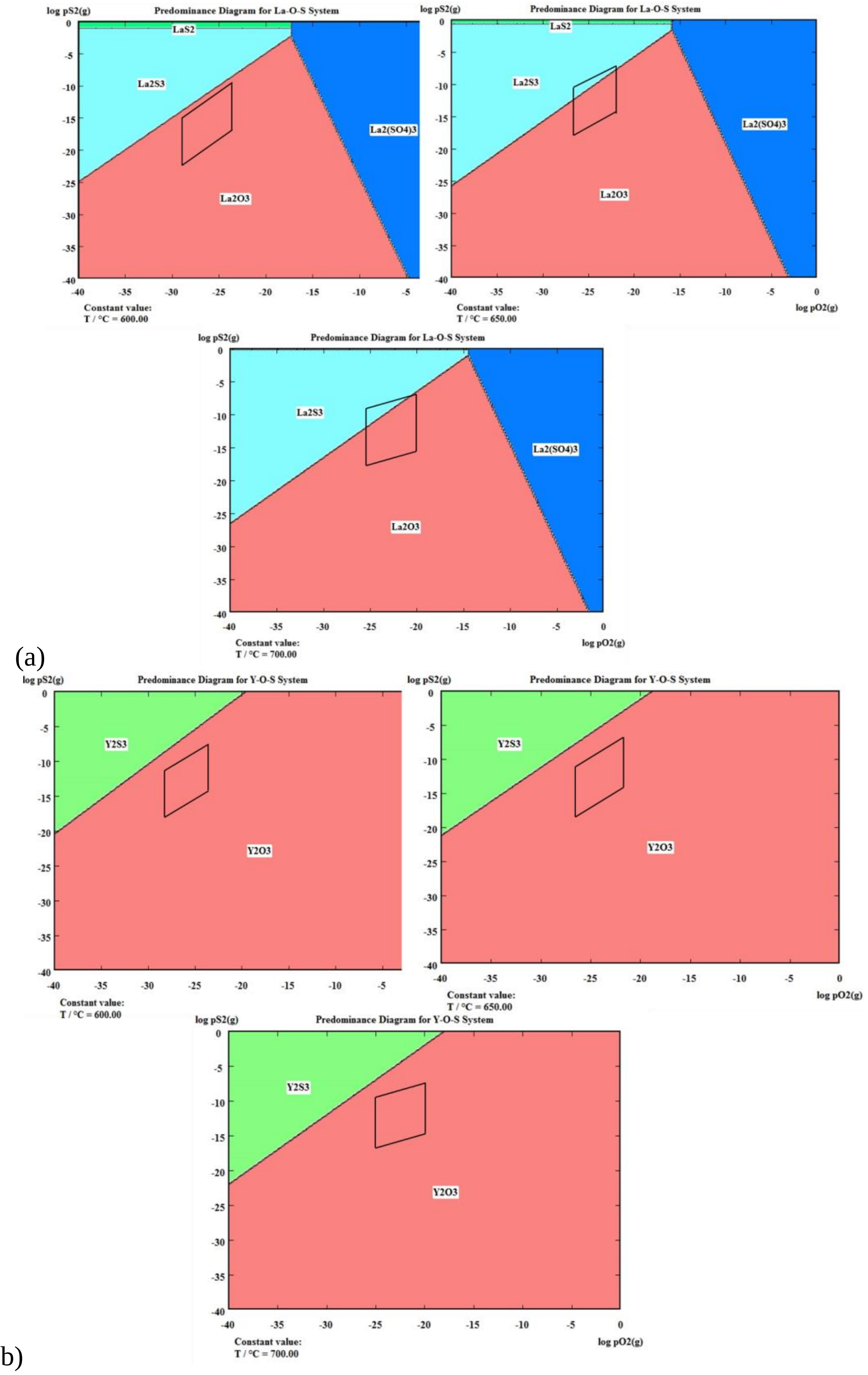

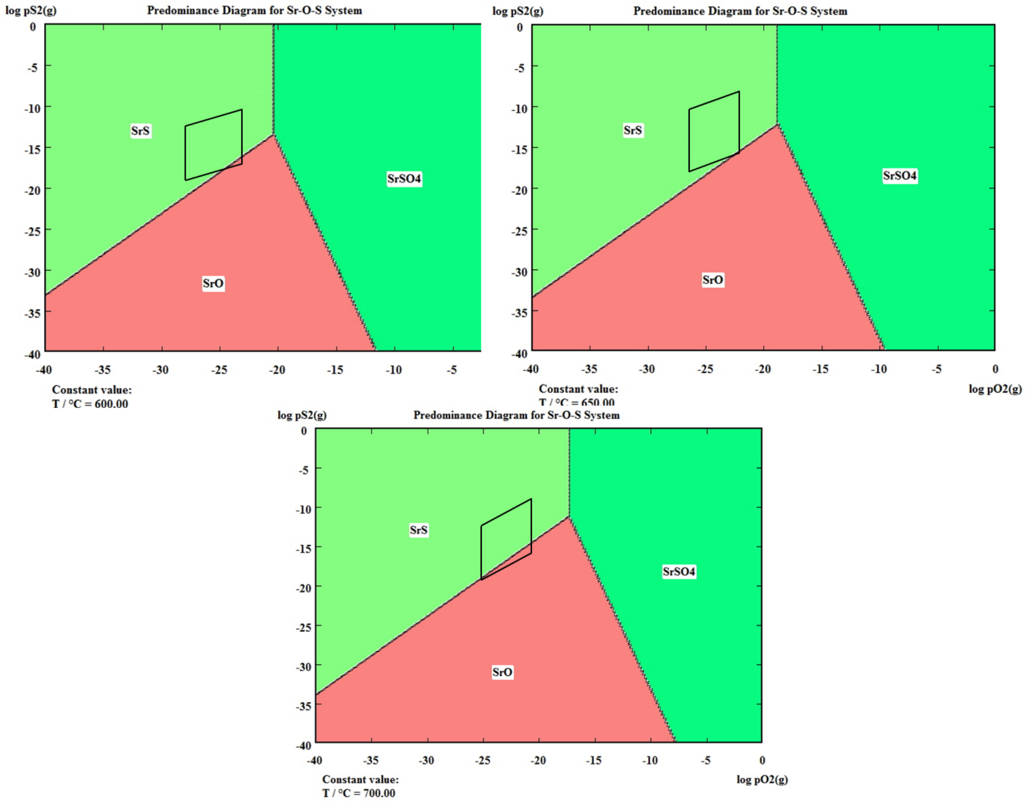
Predominance Diagram for Sr-O-S System
log pS2(g)
log pO2(g)
SrS
SrSO4
SrO
0
-5
-10
-15
-20
-25
-30
-35
-40
Constant value:
T / °C = 600.00
T / °C = 650.00
T / °C = 700.00

(c)

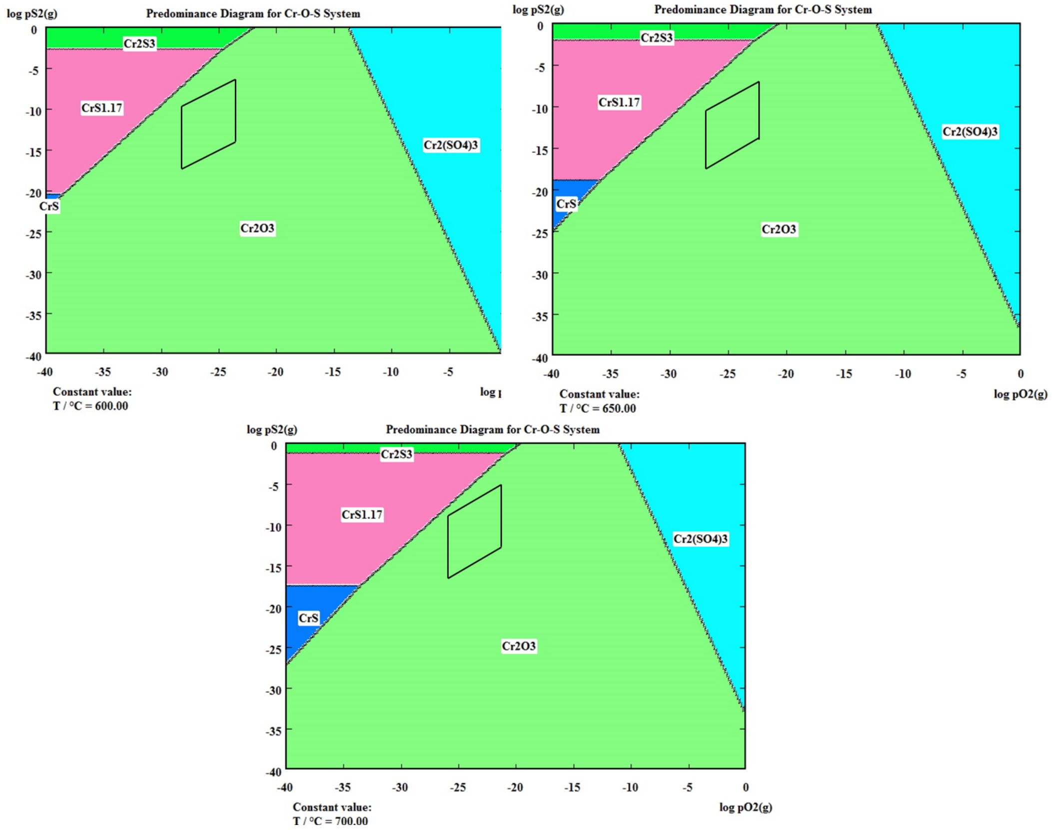
Predominance Diagram for Cr-O-S System
log pS2(g)
log pO2(g)
Cr2S3
CrS1.17
CrS
Cr2(SO4)3
Cr2O3
0
-5
-10
-15
-20
-25
-30
-35
-40
Constant value:
T / °C = 600.00
T / °C = 650.00
T / °C = 700.00

(d)

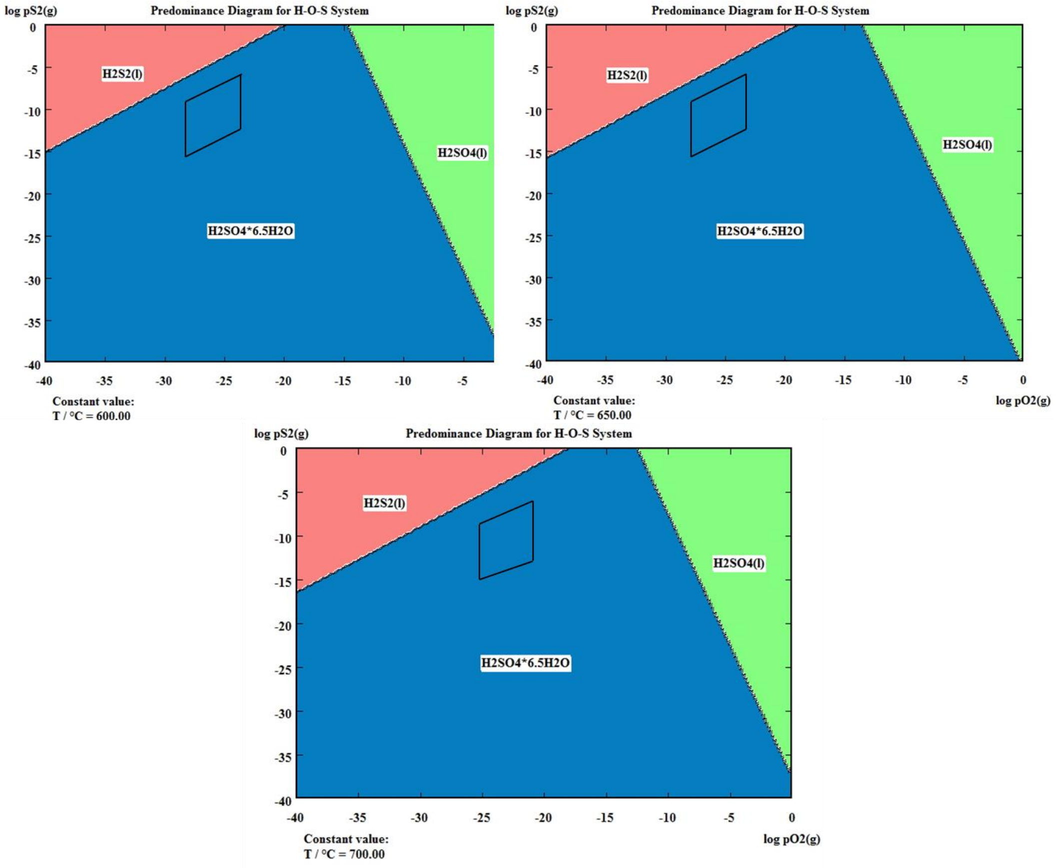

(e)

Figure 8. The phase equilibrium of (a): La-O-S; (b): Y-O-S, (c): Sr-O-S, (d) Cr-O-S and (e): S-O-H systems at 600, 650 and 700 ℃

The pO_2 value was calculated with the correction between the partial pressure of gases and the equilibrium constant of the reaction:

$2H_2(g)+O_2(g)\rightarrow 2H_2O(g)$

The pS_2 value was calculated using the correlation between the partial pressure and the equilibrium constant of the two main reactions:

$2H_2S(g)+O_2(g)\rightarrow S_2(g)+2H_2O(g)$

$2H_2S(g)\rightarrow S_2(g)+2H_2(g)$

Figure 8 indicated that the elements of Y and Cr were stable while La and Sr were easy to be sulfured when exposed in 10% H_2-1% H_2S at the operating temperatures, which suggested that sulfur at this level will affect the bulk properties of the LYSC13 anode. The replacing of La^{3+} or Y^{3+} in A-site by lower valence Sr^{2+} in the pervoskite structure could produce oxygen vacancies [25]. Figure 8a and 8c indicated that SrS and LaS would appear at the operating atmosphere, but the XPS patterns showed that there was no sulphide generation and the S-XPS manifested some SO_4^{2-} appeared, which was consistent with Figure 8(e). In addition, the reaction of sulfur on the surface needed to be considered, which would affect the electrocatalytic activity. Therefore, XPS spectra were used to analyse the state of each surface element.

XPS spectrum was used to characterize the surface characteristics of synthesized sample (LYSC13) before and after test in the 10% H_2-1% H_2S. To quantify the oxidation states La, Y, Sr, Cr and O, the La3d$^{5/2}$, Y3d$^{5/2}$, Sr3d$^{5/2}$, Cr2p$^{3/2}$, and O1s were studied. Table 2 showed the binding energy of La, Y and Sr. Strong electron orbital-spin angular momentum interactions caused a splitting of La XPS peaks.

Table 2. The bond energies of La 3d, Y 3d and Sr 3d

Samples	**La (eV)**		**Y (eV)**		**Sr (eV)**	
	3d$^{5/2}$	**3d$^{5/2}$**	**3d$^{5/2}$**	**3d$^{5/2}$**	**3d$^{5/2}$**	**3d$^{5/2}$**
LYSC13 before test	833.8	837.4	156.8	158.8	131.9	134.1
LYSC13 after test	833.7	837.3	157.0	159.0	132.8	134.4

Form the Table 2, it could be seen the peak of La 3d almost had no change after single cell test in 10% H_2-1% H_2S-N_2. The position of La 3d$^{5/2}$ was located at 833.76 eV and 837.39 eV indicating that the oxidation state was +3 which was in a good agreement with the report in [Ref 15]. Y 3d$^{5/2}$ peak located at 156.82 eV indicating that the oxidation state was +3 which agreed with the [Ref 7 and Ref 8]. The bond energies of Sr increased after cell test, which indicate the change of environment around it. On the other hand, degradation of the electrochemical oxygen exchange kinetics was often connected to Sr enrichment in the surface for tiny amounts of SrO deposing on the material surface and leading to severe deactivation. Meanwhile, B-site, transition metal can cause (re-)activation [26]. So B-site, XPS patterns of Cr 2p3/2 (before and after cell tests) were considered as shown in Figure 9. Cr(Ⅲ) in fresh LYSC13 before test was evidenced by a shoulder observed on the main peak at 576.39 eV (Figure 9a). The coexistence of Cr(Ⅲ) and Cr(Ⅳ) after cell test was evidenced by a shoulder observed on the main peak at 575.6 eV (Figure 9b), which was assigned to Cr(Ⅳ) species. The higher binding energy (BE) Cr 2p1/2 peak at 587.33 eV and its shakeup satellites were due to Cr(Ⅳ). The result was in consistence with the result of HRTEM (as shown in Figure 3b).

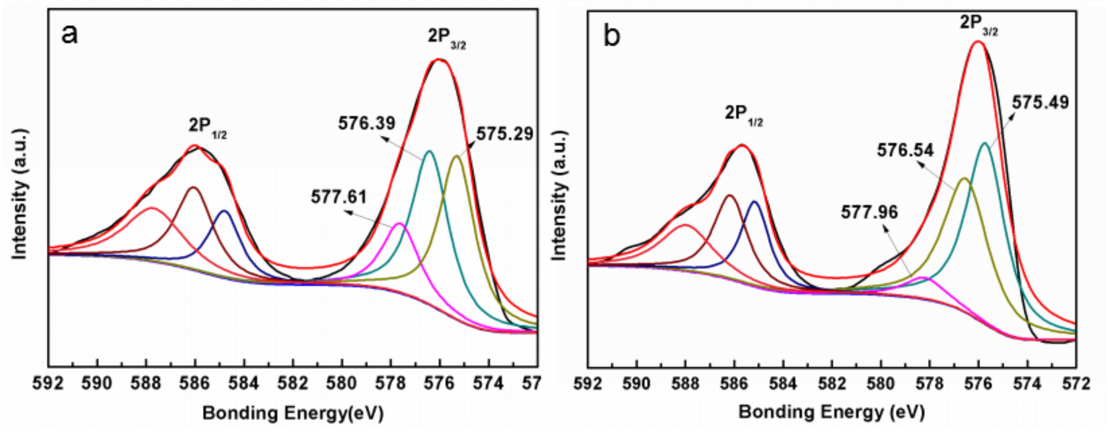

Figure 9. XPS for elements of Cr 2p$^{3/2}$ (a) before and (b) after cell tests in 10% H_2-1% H_2S for 2 h

Oxygen bound to metal played a crucial role in metal oxide catalysts. Table 3 shows O1s spectrum was usually used to analyze the types of oxygen species presented in a particular oxide. As observed from the material, the O1s core level consists of two components. The low B.E. component corresponded to the lattice oxygen (O_β) and the high B.E. had been assigned to surface adsorbed oxygen (O_α). The relative percentage of lattice and adsorbed oxygen were listed in Table 3. The percentage values were calculated from the area of the corresponding peaks. The first peak (529.19-529.24eV) was attributed to the oxygen ions in the crystal lattice (O^{2-}); the second peak (observed at 531.8-531.87eV) was assigned to surface adsorbed oxygen species (O^{2-} or O^{-}). OH groups and oxygen vacancies [27]. Table 3 indicated the O_β decreased after the cell test and corresponding O_α increased which showed the content of the oxygen vacancies increased. The results were in agreement with the XPS spectrum of Cr as shown in Figure 9.

Table 3. The bond energies of O 1S

Samples	**O (eV)**			
	O_β		**O_α**	
LYSC13 before test	529.2	46.10%	531.9	53.90%
LYSC13 after test	529.2	46.08%	531.8	53.92%

The S_{2p} peaks at lower binding energies were assigned to S^{2+}, S^{4+}, S^0 and S^{2-}. After the test of the single cell in H_2S at 700 ℃, the sulfur content was detected and finding out the three peaks located at 168.80, 169.43 and 170.23 eV were mainly attribute to SO_4^{2-} as shown in Figure 10(a). Figure 10(b) gave the schematic diagram of principle about the single cell as H_2S as anode gas. H_2S and generated H_2O, SO_2 were adsorbed on the anode surface, under catalysis of anode material, the three gases continued to be oxidized to sulfate. The result was in accord with the XPS results. The peaks of SrS and LaS didn't appear while some $SrSO_4$ was generated according the Reference [9, 28].

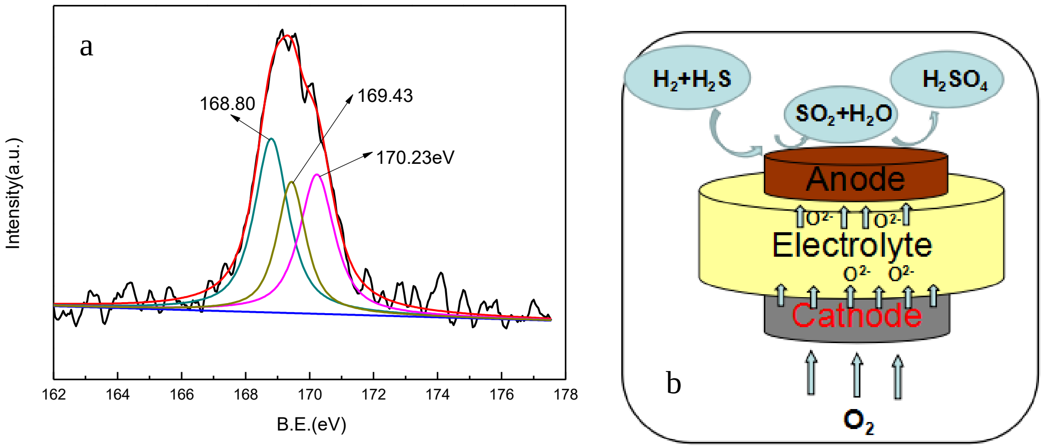

Figure 10. (a) XPS for S element and (b) the schematic diagram of principle about the single cell

4. CONCLUSIONS

According to the XRD spectra and H_2-TPR curves, Y-dopant with x=0.13 was chosen as the research object. LYSC13 as anode material had shown promising performance under 10% H_2-0.1% H_2S. The XRD patterns, SEM and HRTEM indicated that LYSC13 had perfect single crystal structure. HRTEM showed the relatively high intensity streaks along [111] in the [110] diffraction pattern were observed for some grains, which would be regarded as B-site cation (Cr(Ⅲ) and Cr(Ⅳ)) ordering for the overlap of stacking fault-derived scattering, or as the ordering of oxygen vacancies, which were in agreement with the XPS results. For the cell configuration of LYSC13-SDC/SDC/Ag, the maximum power density was 62.66 mW·cm^{-2} and the maximum OCV was 0.96 V under operating atmosphere at 700 ℃. The EIS manifested that the polarization resistance was main loss. XPS indicated that after single cell test, sulfates were formed.

ACKNOWLEDGMENTS
This work was supported by the Natural Science Foundation of Jiangsu Province, China (Grant No. BK20160425 and BK20160424), the Founds of Jiangsu Provincial Engineering Laboratory for Advanced Materials of Salt Chemical Industry (SF201409 and SF201606), Foundation of Huaiyin Institute of Technology (HGC1312 and HGB1203), the National Natural Science Foundation of China (Grant No. 51602118).

References

1. A. Jun, J. Kim and G. Kim, *J. Mater. Chem. A.*, 3 (2015) 15082.
2. Z. Shao, W. Zhou and Z. Zhu, *Prog. Mater. Sci.*, 57 (2012) 804.
3. S. Sengodan, S. Choi, A. Jun, T.H. Shin, Y.W. Ju, H.Y. Jeong, J. Shin, J.T.S. Irvine and G. Kim, *Nature Mater.*, 14 (2014) 205.
4. S. Joo, J. Kim, J. Shin, T.H. Lim and G. Kim, *J. Electrochem. Soc.*, 14 (2016) F1489.
5. L.D. Fan, B. Zhu, P.C. Su and C.X. He, *Nano Energy*, 45 (2018) 148.
6. B.C, Steele and A. Heinzel. *Nature*, 414 (2001) 345.
7. Y. Chen,Y.F. Bu,Y.X. Zhang, R.Q. Yan, D. Ding, B.T. Zhao, S. Yoo, D. Dang, R.Z.Hu, C.H. Yang and M.L. Liu, *Adv. Energy Mater.*, 2017, DOI: 10.1002/aenm.201601890
8. Y.F. Bu, Q. Zhong, D.D. Xu, X.L. Zhao and W.Y. Tan, *J. Power Sources*, 250 (2014) 143.
9. Y. F. Bu, Q.Zhong, D.D.Xu and W.Y. Tan, *J. Alloy. Compd*., 578 (2013) 60.
10. D. D. Xu,Y. F. Bu, W.Y. Tan and Q. Zhong, *Appl. Surf. Sci*., 268 (2013) 246.
11. X. F. Zhu, H. Yan and Q. Zhong, *Appl. Surf. Sci*., 257 (2011) 1967.
12. Y. Zhou, X.F. Guan, H. Zhou, K. Ramadoss, S. Adam, H.J. Liu, S. Lee, J. Shi, M. Tsuchiya, D.D. Fong and S. Ramanathan, *Nature*, 534 (2016) 231.
13. S. Tao and J. T. S. Irvine, *Nature Mater.*, 2 (2003) 320.
14. R. Mukundan, E. L. Brosha and F. H. Garzon, *Electrochem. Solid-State Lett.*, 7 (2004) A5.
15. Y.F. Bu, D. Ding, S.Y. Lai D.C. Chen, X.H. Xiong, T. Wei and Q. Zhong, *J. Power Sources*, 275 (2015) 808.
16. K.J.Yoon, C.A.Coyle and O.A. Marina, *Electrochem. Commun.*, 13 (2011) 1400.
17. Y.F. Bu, Q. Zhong, D.C. Chen, Y. Chen, S.Y. Lai, T. Wei, H.B. Sun, D. Ding and M.L. Liu, *J. Power Sources*, 319 (2016) 178.
18. W.Y. Tan, H. Yan, D.D. Xu and Q. Zhong, *Int. J. Hydrogen Energ.*, 38 (2013) 16552.
19. Y. Zheng, C.M. Zhang, R. Ran, R. Cai, Z.P. Shao and D. Farrusseng, *Acta Materialia*, 57 (2009)

1165.
20. Q. Liu, D. E. Bugaris, G.L.Xiao, M. Chmara, S.G. Ma, H. C. Loye, M. D. Amiridis and F. L. Chen, *J. Power Sources*, 196 (2011) 9148.
21. Z.Q. Deng, J.P. Smit, H. J. Niu, G. Evans, M.R. Li, Z.L. Xu, J.B. Claridge and M.J. Rosseinsky, *Chem. Mater.*, 21 (2009) 5154.
22. E. Bucher, W. Sitte, I. Rom, I. Papst, W. Grogger and F. Hofer, *Solid State Ionics*, 152 (2002) 417.
23. W.J. Weber, C.W. Griffin and J.L. Bates, *J. Am. Ceram. Soc.*, 70 (1987) 265.
24. P. Lohsoontorn, D. Brett and N. Brandon. *J. Power Sources*, 175(2008), 60.
25. S. Tao, J.T.S. Irvine and S.M. Plint, *J. Phys. Chem. B.*, 110 (2006) 21771.
26. G. M. Rupp, A. K. Opitz, A. Nenning, A. Limbeck and J. Fleig, *Nature Mater.*, 16 (2017) 640.
27. K. Jirátová, J. Mikulová, J. Klempa, T. Grygar, Z. Bastl and F. Kovabda, *Apply. catal. A: Gen.*, 361 (2009) 106.
28. A.J. Ma, S.Z. Wang, C. Liu, H. Xian, Q. Ding, L. Guo, M. Meng, Y.S. Tan, N. Tsubaki, J. Zhang, L.R. Zheng and X.G. Li, *Appl. Catal. B. Environ.*, 146 (2014) 24.